Sentinel-1 Wave Mode SAR Monitoring of Icebergs around the Antarctica

Chen Wang[a,b], Xiao-Ming Li[c,d,*], Li-Jian Shi[b], Hui-Min Li[a,b], Alexis Mouche[e], Bertrand Chapron[e]

[a]*School of Marine Sciences, Nanjing University of Information Science & Technology, Nanjing 210044, China*
[b]*Key Laboratory of Space Ocean Remote Sensing and Application, Ministry of Natural Resources, Beijing 100081, China*
[c]*Hainan Aerospace Technology Innovation Center, Wenchang 571333, China*
[d]*Key Laboratory of Digital Earth Science, Aerospace Information Research Institute, Chinese Academy of Sciences, Beijing 100094, China*
[e]*IFREMER, Univ. Brest, CNRS, IRD, Laboratoire d'Oceanographie Physique et Spatiale (LOPS), Brest, France*

Abstract

The high-quality global wave mode synthetic aperture radar (SAR) vignettes routinely collected by Sentinel-1 is today extensively exploited for various oceanic and atmospheric phenomena. Yet, these observations still remain largely untapped for iceberg monitoring in the Southern Ocean. As a follow-up to our previous work (Wang et al., 2019b), a dedicated SAR image classifier is built to detect small-sized icebergs (<5 km) that are commonly underrepresented in current recording systems. It has been fine-tuned from the Inception-v3 deep convolutional neural network using a curated dataset of 2,062 iceberg and 15,338 non-iceberg cases. Independent evaluations, based on three additional datasets, achieve high precision and recall rates above 90%. Applied to all WV images acquired between 2016 and 2018 unveils iceberg occurrences around Antarctica. About ~7.5% of the detected icebergs drift into 40°S to 50°S latitudes, while the majority are concentrated poleward of 55°S. The seasonal patterns of SAR icebergs are generally consistent with altimeter-detection estimates, and exhibit advances over the sea ice regions. Linking these SAR icebergs to the reported large icebergs reveals that small icebergs are more likely located to the east of large iceberg trajectories, suggesting the primary driver of underlying ocean currents to their drift. Although precise identification of the shape and position of these small icebergs remains challenging, WV SAR vignettes provide added values to iceberg investigations at scales beyond current operational reports. Not only relevant for the precise monitoring of icebergs across a wider range of sizes, it can become instrumental for our understanding of iceberg tracking, associated dissolution, along with freshwater transport, and their broader impact on global and local climate processes.

Keywords: Antarctica, Iceberg, Synthetic aperture radar, Sentinel-1 wave mode, Classification

Highlights

- Global Sentinel-1 wave mode SAR aids monitoring of small icebergs around Antarctica
- A deep-learning-based model is developed to identify SAR images containing icebergs
- Icebergs are common in the Southern Ocean with unignorable proportion reaching over 50°S
- Linking small and large icebergs benefits understanding of ocean currents and dynamics

1. Introduction

Icebergs, as drifting remains of calving events from glaciers and ice shelves, are a common phenomenon in the Southern Ocean (Jacobs et al., 1992; Smith, 2011; Tournadre et al., 2016). They are not only indicators of polar ice dynamics but also active entities in influencing sea level, ocean circulation, and marine ecosystems (Biddle et al., 2015; Merino et al., 2016). The trend of global warming has led to a growing mass loss of the Antarctic ice sheet, most of which ending up with calved icebergs (Mackie et al., 2020; Schloesser et al., 2019). Approximately 130,000 icebergs are estimated to be floating around the Antarctic in the austral summer based on 30 years of ship reports, with their dissolution rate dependent on the size and distance from their origins (Orheim et al., 2023b,a). Given this large population, an accurate representation of the iceberg dissolution process in global circulation models has become crucial to characterize its contribution to sea level rise and local circulation pattern, among others (Smith, 2011; Collares et al., 2018; England et al., 2020; Starr et al., 2021).

Means to monitor icebergs have continuously been evolving over the last decades. Most straightforward are reports from sailing ships with iceberg position, shape, size, and volume estimation (Jacka and Giles, 2007; Romanov et al., 2012). They have been a primary data source for iceberg statistics since the last century and continue to provide valuable perspectives on the distribution and dissolution of icebergs (Orheim et al., 2023b; Romanov et al., 2017). Meanwhile, satellite measurements have been demonstrated for monitoring icebergs over the most remote regions on Earth (Smith, 2011). Optical sensors provide high-resolution and detailed visual images

*Corresponding author
Email address: lixm@radi.ac.cn (Xiao-Ming Li)

to identify icebergs (e.g. Braakmann-Folgmann et al., 2021), but are restricted by cloud cover and the absence of daylight during polar winters. Microwave instruments, by comparison, are not hindered by weather conditions. The scatterometer worked as a popular means for iceberg detection based on the higher backscattering in contrast to the background water (Stuart and Long, 2011). Given the continuous operation of scatterometers, an operational database for tracking large iceberg (larger than 6 km in length) has been compiled and updated (Budge and Long, 2018). Beyond its well-known capability for sea level measurements, spaceborne altimeters have also been demonstrated to capture iceberg signatures through the thermal noise signal analysis in open water (Tournadre et al., 2008). A complementary database of smaller-size icebergs composed of their position, size and volumes has then been created combining multiple altimeter satellites (Tournadre et al., 2012, 2016). Yet, it is worth pointing out that the size of icebergs is estimated based on assumptions of fixed backscattering and free-board elevations (Tournadre et al., 2012) in addition to the fact that the shape of icebergs is also hard to infer from altimeter measurements.

Spaceborne synthetic aperture radar (SAR) serves as a good candidate for complementary monitoring of all-sized icebergs attributed to its relatively wide coverage and high spatial resolutions (Barbat et al., 2019, 2021; Braakmann-Folgmann et al., 2022; Evans et al., 2023; Koo et al., 2023; Mazur et al., 2017; Power et al., 2001; Silva and Bigg, 2005; Wesche and Dierking, 2015; Young et al., 1998). Similarly to scatterometers, SAR relies on backscattering of the illuminated surface to identify the presence of icebergs. The radar backscattering over icebergs is a combination of surface scattering and volume scattering, often higher than the open water and visualized as bright objects on SAR images. One of the ever-largest icebergs on record calved from the Larsen C Ice Shelf in 2017, A68, has been consistently monitored by SAR in terms of its subsequent breakup as well as the drift during its lifecycle (Braakmann-Folgmann et al., 2022; Smith and Bigg, 2023). Thanks to the consistent acquisition plan of Sentinel-1 (S-1) across the Arctic region, an added-value product is operationally delivered by the Copernicus Marine Environment Monitoring Service with the full name of "SAR Sea Ice Berg Concentration and Individual Icebergs Observed with Sentinel-1". However, most of the relevant studies focus on automated detection of large icebergs based on wide-swath SAR images acquired in coastal areas where they are present all year round (Marino et al., 2016; Karvonen et al., 2021; Evans et al., 2023). Although icebergs of different sizes are equivalently significant, giant icebergs are better represented in climate models as they received much more attention (for example, the NIC iceberg database only reports iceberg larger than 18.5 km along at least one axis) (Tournadre et al., 2016).

By comparison, smaller-sized icebergs (~1 km) remains less tapped due to the lack of solid observational source for characterizing their distribution and melting process. Such situation might be changed by S-1 wave mode (WV) acquisitions that systematically collect SAR vignettes (20 km by 20 km) over the open ocean. The huge amount of this database (60,000 per month per satellite) still poses great challenges to detect and identify small-sized icebergs across the vast Southern Ocean. Wang et al. (2019a,b) marks one of the earliest studies to explore S-1 WV acquisitions for automatic classification of vignettes regarding sea ice and iceberg signatures. While such a multiclass classification model is useful for tagging the whole WV image archive for quick categorization, some limitations are evident. Regarding the iceberg detection, the precision is far from satisfactory (17%) despite of the high recall (93%). Hard-metal objects, like vessels and platforms, have been misinterpreted that leads to a degraded classification performance (Wang et al., 2019b). This is because the overall features are not sufficient to represent the differences between icebergs and the metal objects for this comprehensive model, dealing with 10 classes, from pure ocean waves to oceanic front (Wang et al., 2019b).

This study aims to demonstrate the use of a more dedicated binary classification model focusing on iceberg (IB) and the other non-iceberg (NIB) images. We first built a hand-crafted database of 17,400 labeled S-1 WV vignettes containing various iceberg signatures in terms of their size, shape and radar backscattering contrast relative to the surrounding water. It is divided into two part for training and validating the classification model to achieve optimal performance, respectively. This model is then applied to a three-year SAR dataset for further geophysical analyses of the detected small-sized icebergs. Results presented here are demonstrated to bridge the gaps between large and small-sized icebergs for better understanding the breakup and melting during their entire lifecycle.

The remaining of this paper is organized as follows. The datasets are described in Section 2, including S-1 WV SAR vignettes and auxiliary environmental variables used in this study. The IB classifier (CMwvIB) is trained and evaluated in Section 3. Its application and analysis to a three-year period of SAR acquisitions around the Antarctica are illustrated in Section 4. Discussion and conclusion are given in Section 5.

2. Datasets and processes

2.1. S-1 WV SAR images

The Sentinel-1 (S-1) mission comprises a polar-orbiting, sun-synchronous Synthetic Aperture Radar (SAR) satellite constellation designed for long-term monitoring of open ocean (Torres et al., 2012). S-1 satellites cross the equator at approximately 6:00 AM in descending orbit and 6:00 PM in ascending orbit, ensuring consistent global coverage. The revisit cycle is 12 days per satellite, which can be reduced to 6 days with two satellites in orbit. S-1A and S-1B were launched in 2014 and 2016, respectively and S-1B mission has unfortunately come to an end in December 2021 due to an anomaly in its electronics power supply. Such an observational capacity shall be restored by the upcoming launch of S-1C expected in 2024 and the Harmony mission in 2029.

After its in-orbit commissioning phase, Wave Mode (WV) began its routine acquisition of SAR vignettes in June 2015 for S-1A and in June 2016 for S-1B, respectively. To our knowledge, it is the only imaging mode that operationally acquires vignettes over the global open oceans. Approximately 65,000 scenes are acquired per month per satellite, each covering a 20 km by 20 km swath with a pixel spacing of 5 m. These vignettes are collected by default in VV polarization (HH polarization was temporarily operational for S-1B between 15 March and 1 July 2017) at two alternating incidence angles of 23.5° (termed as WV1) and 36.5° (termed as WV2). This “leapfrog” acquisition pattern results in a separation of 200 km between two consecutive WV images at the same incidence (Fig. 1). All WV SAR vignettes are publicly accessible via ESA Sentinel Open Access Hub (`https://sentinel.esa.int/web/sentinel/sentinel-data-access`) and are also archived by the French Research Institute for Exploitation of the Sea (IFREMER) at `http://www.ifremer.fr/datavore/exp/dvor/#/s1quicklook`.

In this study, we focus on the area from 40°S poleward as it is widely acknowledged that icebergs barely go further north (Tournadre et al., 2016). S-1 switches its acquisition mode to wide swath (either interferometric wide or extra wide) approaching the Antarctic continents in terms of the Mission Operation Scenario for dedicated sea ice observations. Top left of Fig. 1 illustrates the spatial locations of ~5700 WV images collected within one revisit cycle of 12 days (blue dots for WV1 and red dots for WV2). The monthly count of WV SAR vignettes across a 2° by 2° grid can reach up to 40, as shown by the color-coded distribution in top right of Fig. 1. The spatial pattern of these acquisitions effectively overlaps with regions identified as frequent occurrence of icebergs (Tournadre et al., 2008, 2016). IBs in these regions should thus be readily detectable and well-resolved within the high-resolution WV SAR vignettes, especially for the calved icebergs beyond the reported scope of scatterometers and radiometers.

To enhance the visibility of image patterns, a processing step converting the commonly used normalized radar cross section (NRCS) to the sea surface roughness image is implemented as in (Wang et al., 2019a). This is achieved by dividing SAR-measured NRCS by a referenced NRCS calculated with the empirical geophysical model function CMOD5.N at a constant wind speed and direction (here we take 10 m/s and 45°). Each image is then downsampled to a reduced spatial

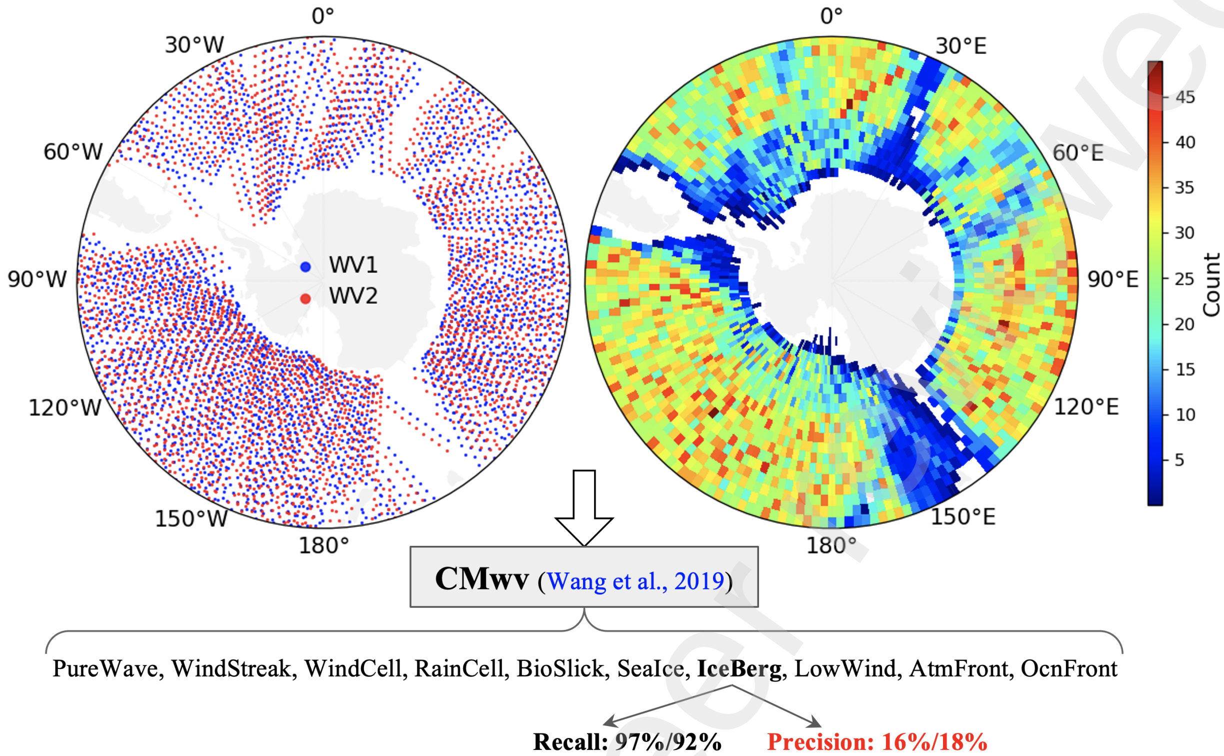

Fig. 1. Top left gives S-1 WV center locations acquired within a revisit cycle between 1 December 2016 and 12 December 2016 for WV1 (blue dots) and WV2 (red dots). Top right is the monthly count of WV vignettes combining WV1 and WV2 in the grid of 2° by 2°. Bottom panel shows the overall recall and precision rate of icebergs given by CMwv developed in (Wang et al., 2019b).

spacing of 50 m from the full resolution of 5 m using a mean filtering. This downsampling step is carried out to not only increase the signal-to-noise ratio, but also reduce the image size for later training input.

2.2. Training and assessment dataset

Our study focuses on developing an iceberg-specific identification model, which requires a robust dataset of labeled WV SAR vignettes for training and evaluation. To this aim, an iceberg and non-IB dataset is constructed by merging two previously established databases: a training dataset containing 37,553 images of ten distinct geophysical phenomena (Wang et al., 2019a), and an assessment dataset (hereafter referred to as AD10k) used to evaluate the performance of the CMwv model presented by Wang et al. (2019b). The former dataset, comprising WV vignettes exclusively from Sentinel-1A acquired throughout 2016, includes 1,980 images labeled as icebergs, previously utilized in the development of CMwv. The AD10k dataset consists of 10,000 randomly selected and labeled Sentinel-1A WV SAR images from 2016, of which 109 images exhibit distinct iceberg features, with 27 overlapping with the training dataset. Note that both datasets are count-equalized between WV1 and WV2 acquisitions, ensuring that the influence of varying SAR incidence angles on iceberg detection and identification, as discussed by Wesche and Dierking (2012), can be neglected.

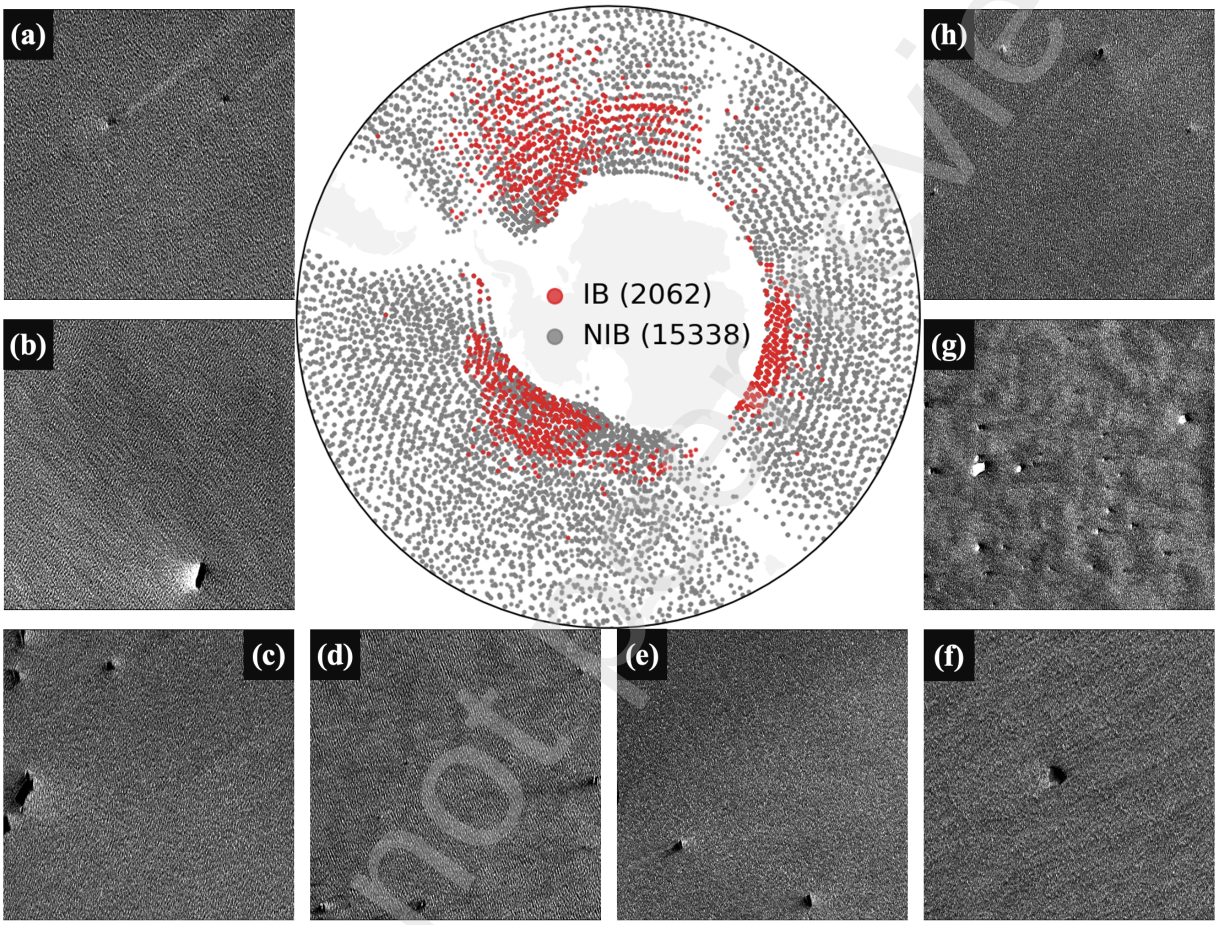

Fig. 2. Map plot of the labeled iceberg (IB) and non-iceberg (NIB) images assembled for training of the classification model (CMwvIB). Eight cases are given to illustrate the various shapes and patterns of SAR-observed IBs.

Given the fact there is no record of icebergs drifting northward of the latitude 40°S, SAR images with central locations northward 40°S are excluded from the newly combined database, leading to 17400 vignettes in total. The central map in Fig. 2 provides a comprehensive overview of the spatial distribution of the dataset used in this study, which includes 2,062 iceberg (IB) and 15,338 non-iceberg (NIB) labeled S-1 WV SAR vignettes. The IB vignettes are represented by red dots, and the NIB vignettes by gray dots. The map clearly shows that the majority of IB samples are concentrated in the Weddell Sea and the eastern sector of the Southern Ocean, regions known for their high iceberg activity (Tournadre et al., 2012). This distribution is consistent with previous observations that highlight these areas as hotspots for iceberg formation and drift due to their proximity to calving fronts and strong ocean currents. In contrast, the NIB vignettes are more uniformly distributed across the Southern Ocean, reflecting a broader representation of geophysical phenomena other than icebergs.

Surrounding the map are eight example SAR vignettes, illustrating the diversity of small-sized iceberg appearances captured by SAR images. The vignettes display a range of iceberg sizes and shapes, from small, barely visible dots to larger as in Fig. 2 (g), more distinct features with sharp contrasts against the surrounding ocean surface. This variability highlights the challenges in distinguishing icebergs from other oceanic features, particularly in areas with complex backscattering characteristics such as sea ice, wind streaks, or ocean fronts. Another aspect worth mentioning is that these high-resolution images reveals the distinct scattering mechanisms associated with icebergs, varying between bright and darker radar returns in contrast with the ocean background. This is possibly associated with several impact factors including iceberg size, orientation, and the local radar incidence angle. In addition, for some particular cases such as Fig. 2 (a) and (h), wakes of the movements of small icebergs are visible. This shall likely result in misclassificiation with vessels (Asiyabi et al., 2023), but fortunately Southern Ocean is not a popular shipping route (Schreier et al., 2007).

The dataset was randomly partitioned into two subsets with a 7:3 ratio, where 30% is reserved for testing model performance during the training phase. Additionally, three independent datasets (referred to as AD1, AD2, and AD3) are constructed to further evaluate the performance and sensitivity of the CMwvIB model. This multi-dataset approach is critical for validating the model robustness when applied to extensive WV SAR dataset (LeCun et al., 2015). Each vignette within these datasets was manually labeled by three SAR experts, and the results are cross-validated against the model outputs. Specifically,

- AD1 includes 179,019 S-1A WV images acquired between 0-30°S in 2016, among which no IB is expected.
- AD2 includes 14,732 S-1A WV images acquired poleward of 40°S during January 2017 (austral summer) where both IB and NIB are labeled, with a higher frequency of IB expected.
- AD3 includes 18,005 S-1A WV images acquired poleward of 40°S in July 2017 (austral winter) with IB and NIB both labelled with fewer IB expected.

2.3. *Auxiliary data*

To examine the relationship between the identified icebergs and larger icebergs, we use the consolidated Antarctic IB tracking database from Brigham Young University and the National Ice Center (BYU/NIC) (Budge and Long, 2018). This dataset, accessible at `https://www.scp.byu.edu/data/iceberg/database1.html`, consists of two primary files. The first file includes the original BYU daily IB tracks derived from various scatterometer measurements and interpolated NIC IB positions, mostly obtained from optical, infrared, and SAR sensors. The second file provides daily unique IB tracks, generated by averaging the positions from multiple sensors. Both files also contain data on iceberg sizes (>6 km for BYU and >18.5 km for NIC in length or >5 km^2), rotation angles, and masking flags for each IB. In this study, we only focus on the IB positions from the daily unique tracks.

To complement the seasonal manifestation of the identified icebergs, we include the sea ice concentration product which is publicly available at `ftp://ftp.ifremer.fr/ifremer/cersat/products/gridded/psi-concentration/`. This product is derived from Special Sensor Microwave Imager (SSM/I) radiometer (Ezraty et al., 2007) and has been operational since 1992 with a spatial resolution of 12.5 km. We use the monthly data to generate seasonal sea ice concentration maps, from which the sea-ice boundaries defined by the 10% contour is then derived.

3. Development of the iceberg classifier

This section details the development, training, and evaluation of the built CMwvIB model, an iceberg-specific classifier extended from previous CMwv framework that effectively categorized global WV SAR imagery into ten common geophysical phenomena (Wang et al., 2019b). The primary objective is to refine the classification of iceberg and non-iceberg features by fine-tuning Google's Inception-v3 convolutional neural network (CNN). Although this represents a relatively straightforward machine learning task, it serves as an essential step toward applying WV SAR vignettes for specific iceberg studies.

3.1. *Model creation and training*

The Inception-v3 architecture, an evolution of the original GoogLeNet or Inception-v1 model (Szegedy et al., 2015), brings in additional factorization techniques to increase the number of convolutions while maintaining computational efficiency (Szegedy et al., 2016). This architecture has demonstrated exceptional performance, achieving 94.4% top-5 accuracy on the ImageNet Large-Scale Visual Recognition Challenge (ILSVRC) 2012 classification dataset. The

Inception-v3 model was selected for this study due to its proven performance in our previous classification work and its straightforward implementation using the Keras deep learning library (https://keras.io/). The model comprises 48 network layers with approximately 23 million trainable weights, organized into feature extraction and classification components. The feature extraction layers are optimized to detect key image features such as curves, edges, gradients, and patterns, yielding 2048 optimal features to feed the final classification layer of the architecture.

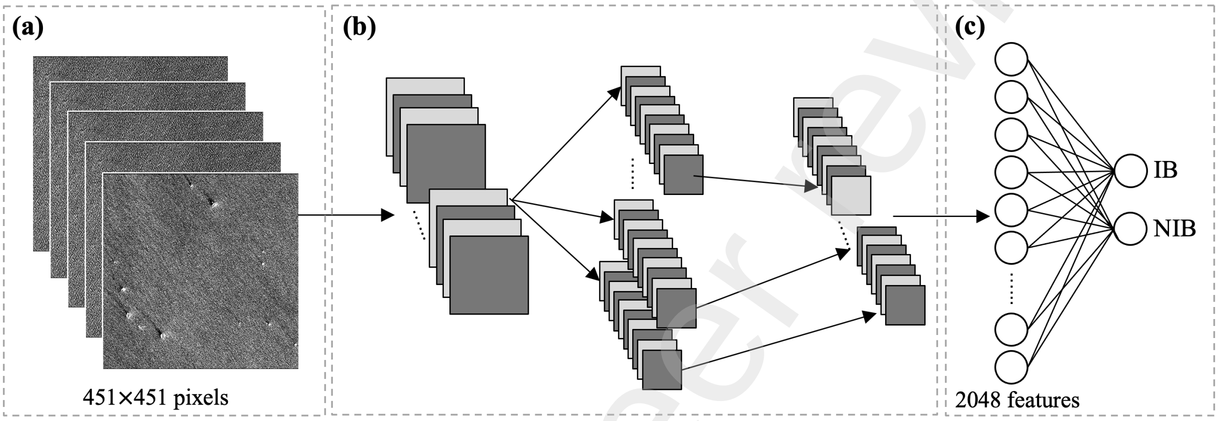

Fig. 3. Schematic representation of the IB classifier (CMwvIB) implemented based on Inception v3 architecture. The input layer is modified to take images with size of 451 × 451 pixels and the output layer returns the probability of an image containing iceberg. The probability of an image classified as IB and NIB summarizes to 1.

For this study, we use the CNN architecture by only modifying the input and output layers, following a previous similar approach Wang et al. (2019b). Specifically, the input layer is adjusted to accept images with dimensions of 451 by 451 pixels, allowing the model to fully capture the content of the downsampled SAR vignettes (Fig. 3). The final layer is replaced by a new classification layer designed to output the probabilities of IB and NIB categories. These probabilities sum to 1 and the model classifies an image as IB if the corresponding score exceeds that of NIB. The remaining layers of the Inception-v3 architecture are retained, with their weights initialized from the CMwv model. Fine-tuning of the entire network is then conducted using 70% of the training dataset, as outlined in Section 2.2. The remaining 30% of the dataset is used for validation at each epoch, ensuring robust model performance during optimization. It is worth noting that the random partitioning of the training and validation subsets does not influence the overall model accuracy, as demonstrated by Fig. 3 in Wang et al. (2019b).

To train the CMwvIB model, the gradient descent optimizer is employed with a learning rate of 0.00001 and a momentum of 0.9. During each epoch, the model processes batches of 32 images and accordingly updates the layer weights. The selected images experience a series of random transformations, including shifts, flips, rotations, and zooms, with newly introduced pixels filled by reflecting adjacent values. This real-time data augmentation approach addresses the challenge of uneven sampling commonly encountered in machine learning classification tasks. To note for operational use of CMwvIB, no further preprocessing of the input images is required.

As shown in Fig. 4 (a), the overall accuracy (OA) of CMwvIB increases rapidly during training, reaching approximately 99% by the 50th epoch. Beyond this point, the OA exhibits minimal fluctuation, peaking at 99.2% at the 426th epoch. The model is fine-tuned over a limited number of epochs, as the OA has already achieved a remarkably high level. Fig. 4 (b) presents the corresponding confusion matrix, where true positives (TP), false positives (FP), false negatives (FN), and true negatives (TN) are defined. From this matrix, the precision (TP/(TP+FP)) and recall (TP/(TP+FN)) for iceberg detection are calculated to be 96.8% and 98.8%, respectively. These metrics manifest a significant improvement in iceberg detection performance compared to the original CMwv model.

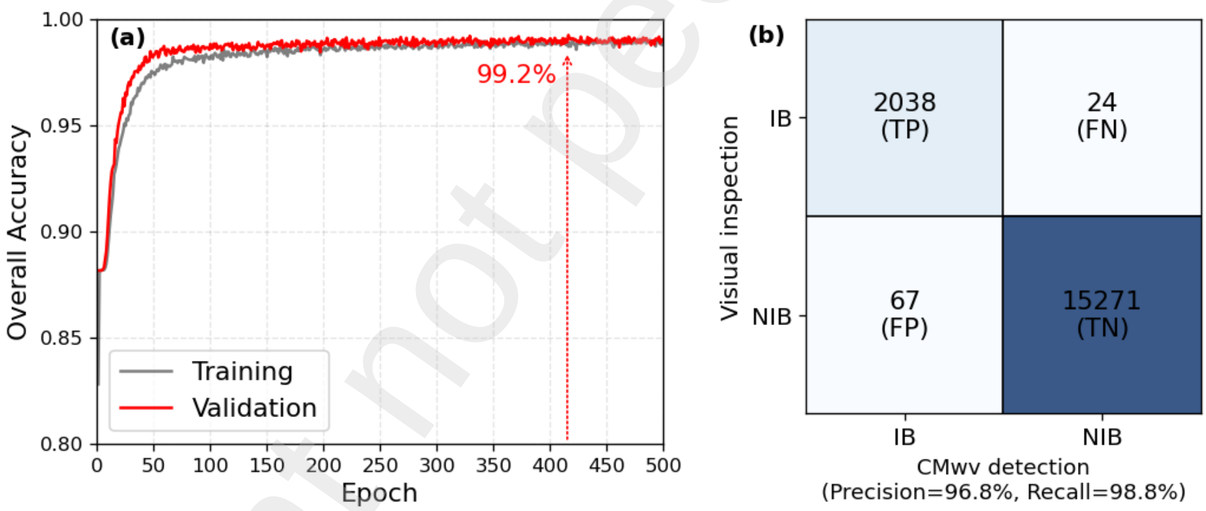

Fig. 4. Performance of the iceberg classifier CMwvIB in terms of its (a) overall accuracy (OA) variation versus epoch during the model training and (b) confusion matrix based on all training images. The vertical arrow in (a) marks the highest OA (99.23%) achieved at the 416th epoch. The letters within parenthesis in plot (b) indicate true positive (TP), false positive (FP), false negative (FN) and true negative (TN), respectively with the precision of 96.8% and recall of 98.8% for iceberg detection.

3.2. Image features extracted by CMwvIB

Performance of the CMwvIB model is tightly linked to the 2048 image features derived through a series of convolutional and pooling layers. These features are fully explored in the final classification layer and help illustrate the architecture behavior. In Fig. 5 (a), these high-dimensional features extracted by CMwvIB are projected onto a two-dimensional plane using the t-distributed Stochastic Neighbor Embedding (t-SNE) technique, as described by Van der Maaten and Hinton (2008). The t-SNE algorithm computes similarities between data points based on joint probabilities, enabling the minimization of the Kullback-Leibler divergence between the original high-dimensional data and its lower-dimensional representation. The embedding map shown in Fig. 5 (a) is generated using all training images, illustrating the pairwise distances between samples. Both IB and NIB classes are well-clustered and can be distinctly separated using a straightforward threshold, such as the dashed line depicted in the plot. The NIB cluster exhibits greater dispersion compared to the IB cluster, reflecting the broader range of phenomena encompassed by the NIB class in WV SAR data. Interestingly, despite being trained to classify only between IB and NIB, the CMwvIB model demonstrates an ability to further subclassify NIB images given the robust capabilities of this Inception-v3 CNN model, as also evidenced by the CMwv framework (Wang et al., 2019b).

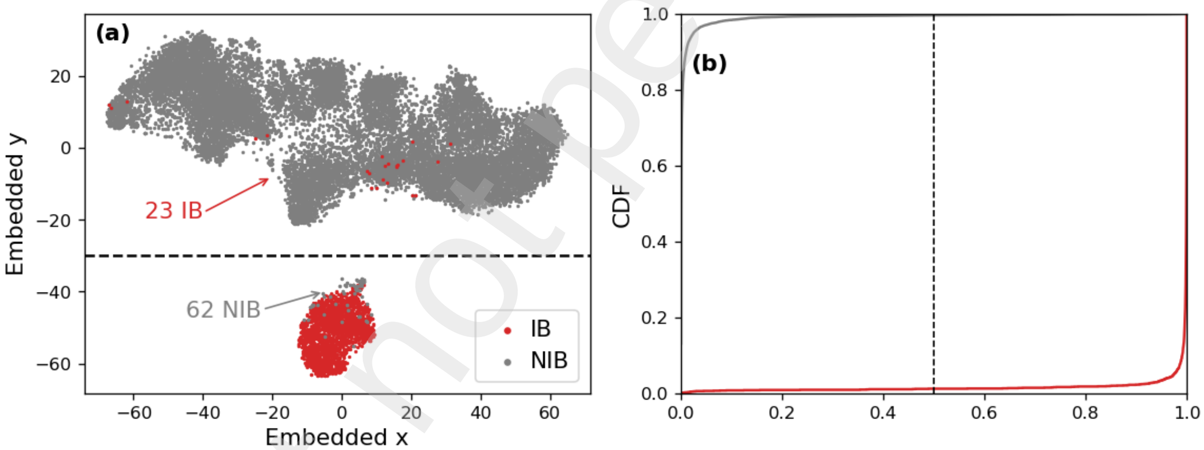

Fig. 5. (a) Projection of the 2048 image features in the trained CMwvIB classifier onto a 2D plane using the t-SNE algorithm for visual inspection. (b) The cumulative distribution function of the probability that an image contains icebergs, as predicted by CMwvIB for the training dataset.

The analysis of the t-SNE embedding reveals a subset of cases where the CMwvIB model classification and visual inspection are inconsistent. That is specifically 62 images labeled as NIB but categorized as IB by the model, while 23 labeled as IB but grouped as NIB by the model. These cases of discrepancy do not precisely correlate with the confusion matrix in Fig. 4 (b) due to the differences between t-SNE dimensionality reduction method and the operation of a fully connected neural network. Playing the built-in parameters of t-SNE algorithm may yield results consistent with the CMwvIB classification, which is beyond the focus of this paper. Nevertheless, the minor deviation observed in these cases has almost negligible impact on the overall classification performance. Fig. 5 (b) demonstrates the distribution of the probability of an image classified as an IB by the model. As expected, the cases labeled as NIB show quite low probability of being grouped as IB that 99.6% of NIBs are below 0.5. This is in contrast with the labeled IB images having high probability that 98.8% of the correctly identified IBs exhibit an IB score above 0.5. Although lowering the threshold might enhance IB detection, it could also increase the rate of false alarms. Therefore, a threshold of 0.5 is consistently applied throughout this study to distinguish between IB and NIB classes.

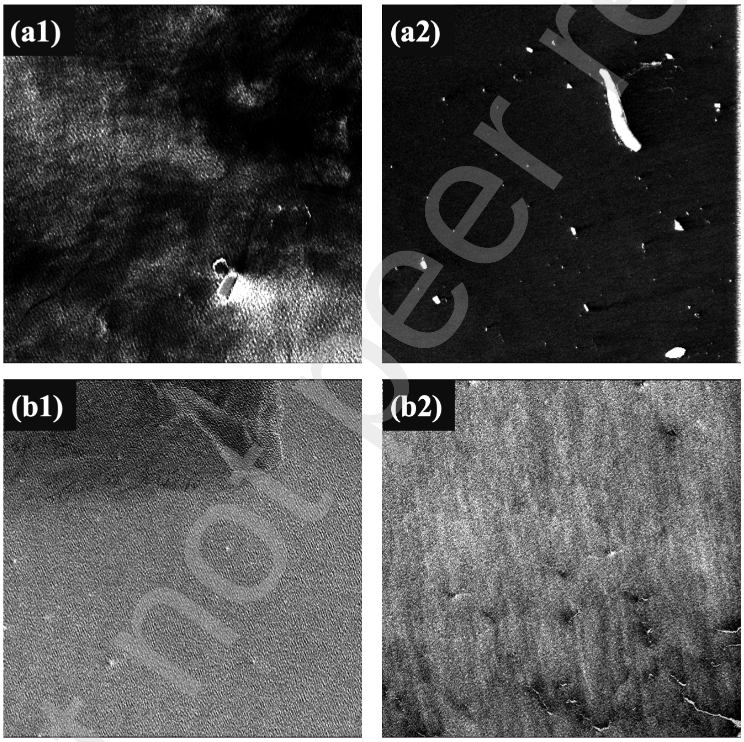

Fig. 6. Demonstration of four inconsistent classification cases between expert labeling and CMwvIB. The top panel features two images labeled as IB but with very low model detection probabilities of 0.03% and 0.15%. The bottom panel displays two cases labeled as NIB that exhibit high model detection probabilities of 99.97% and 80.62%, respectively.

The misclassified cases identified in Fig. 6 are presented to highlight specific challenges in iceberg detection using the CMwvIB model, as shown in Fig. 5 (a). The top two images in Fig. 6 are labeled as iceberg by human experts but are classified as non-iceberg by the CMwvIB model. This misclassification likely results from the model limitations in distinguishing between icebergs and sea ice when they coexist in the same scene. The visual similarity between icebergs embedded within larger sea ice fields and other bright reflectors, such as sea ice floes, can confuse the model. In such cases, the algorithm may be unable to properly weigh the subtle features that differentiate icebergs from sea ice, such as shape, edge contrast, or textural properties, leading to incorrect predictions. The bottom two images in Fig. 6 represent the reverse situation, where the model classified scenes as containing icebergs even though human experts labeled them as non-iceberg. Here, the presence of small icebergs within areas dominated by sea ice likely contributed to the model confusion. The interaction between icebergs and surrounding sea ice introduces additional complexity, as the model may rely on features such as reflectivity or texture, which are similar in both icebergs and sea ice. These factors could lead to an overestimation of the likelihood that an image contains an iceberg.

3.3. Independent assessment

Internal model validation based on a subset of the training dataset aims to help iterate the parameter optimization during the training process. However, the training dataset may not be sufficient to represent all the conditions in WV observations. The model performance must thus be evaulated using independent datasets, such as the three described in Section 2.2. The confusion matrix for each dataset (AD1, AD2, and AD3) are presented in Table 1. For AD1 composed of 179,019 samples acquired in 2016 within the 0–30°S region, all images are expected to belong to the non-iceberg class. And only 1.1% (1,961 images) are misclassified as IB, likely contaminated by rain events or presences of metal objects (vessels, platforms). CMwvIB exhibits satisfactory performance across AD2 and AD3, which include WV SAR images from January and July 2017, acquired 40°S poleward. Precision and recall values exceed 90% across both large datasets (14,732 images in AD2 and 18,005 in AD3). The classifier is relatively better performing during the austral summer, with IB detection misses of 6% in AD2 and 9% in AD3, and false positives of 1% and 8%, respectively. Such a seasonal discrepancy is largely to be attributed to the substantial variations in IB occurrence, e.g. Tournadre et al. (2012). The reduced accuracy in austral winter likely results from difficulties in distinguishing IBs coexisting with sea ice.

To gain insights into the limitations of the CMwvIB classifier, a thorough visual analysis of the misclassified IB and NIB instances is further conducted, focusing exclusively on the false positives (FN) and false negatives (FP) highlighted in Table 1. This double verification procedure is similar to that shown in Fig. 6. For the NIB images misclassified as IB, we find that a significant portion of these cases involved small rain events, characterized by bright and dark spot-like features. This observation aligns with previous findings Wang et al. (2019b), which demonstrated that rain has

Table 1 Performance of the iceberg classifier CMwvIB based on the three independent assessment datasets.

Dataset	TP	FN	FP	TN	Precision (%)	Recall (%)
AD1	0	0	1,961	177,058	0%*	∞*
AD2	1,307	78	18	13,282	99%	94%
AD3	101	10	9	17,869	92%	91%

* Zero detection of IB would lead to 0 precision and ∞ recall based on their definitions.

a substantial impact on IB detection due to its variability and the complex signatures it induces in SAR imagery (Alpers et al., 2016). Additionally, some false positives are caused by features such as islands, ships, and atmospheric phenomena (e.g., dark or bright patches from convective events). For the false negatives (IB misclassified as NIB by the model), most cases occurred in challenging environmental conditions, such as within sea ice zones, areas of very low wind, or regions with heavy rainfall, strong convective cells, gust fronts, and bio-slicks. These phenomena coexist with the distinct local features of IBs, making their accurate detection challenging. Further refinement of the classifier is necessary to improve detection of these less common IB instances.

4. Applications

The application of CMwvIB to S-1A WV SAR data acquired poleward of 40°S during 2016-2018 is carried out to analyze the distribution, relationship with large icebergs, and temporal variation of icebergs in the Southern Ocean. This analysis is, to best of our knowledge, a pioneering effort, concentrating on the statistical evaluation of these WV SAR images to quantify iceberg presence. The observational footprint of the WV SAR images, approximately 20 km by 20 km, must portray the occurrences of small to very small-sized icebergs (<< 10km), compared to scatterometer and altimeter measurements.

4.1. Overall and extremes

CMwvIB identified a total of 19,004 iceberg images from the experimental WV SAR dataset. It is important to note that this figure underestimates the actual number of IBs, as each WV SAR image could potentially contain multiple icebergs. These smaller icebergs are typically fragments that have broken off from larger ice masses due to various factors, documented in previous studies (Huth et al., 2022; Orheim et al., 2023a). Fig. 7 illustrates the frequency of occurrence of

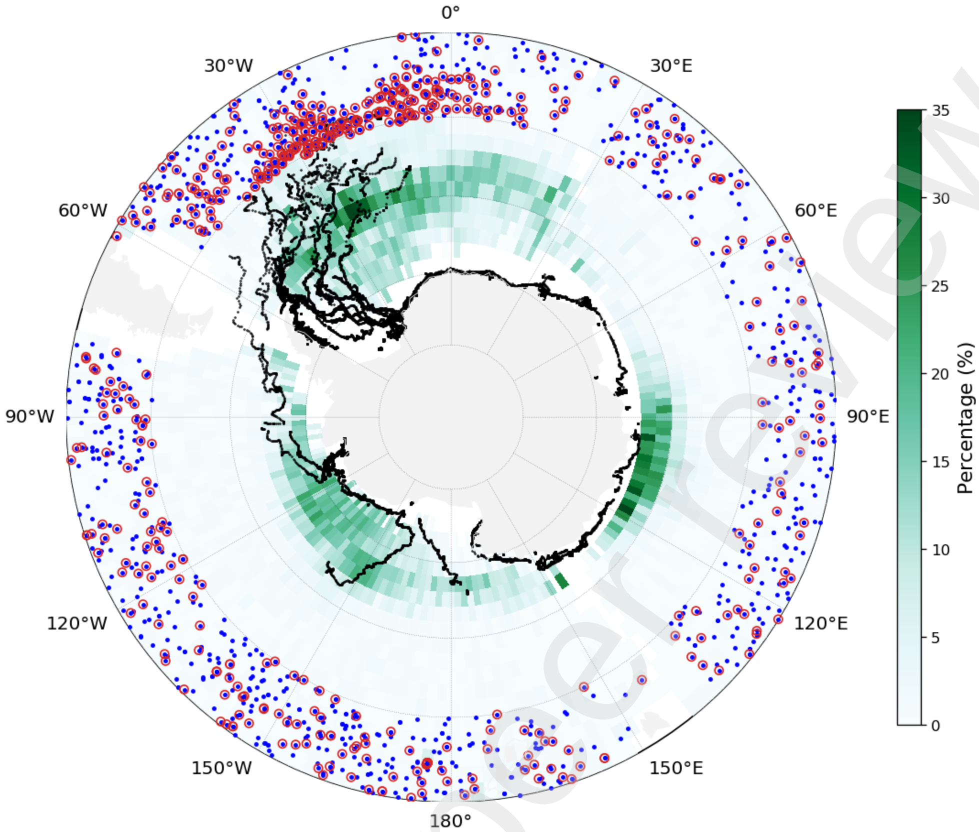

Fig. 7. Percentage of detected icebergs in each 2° by 2° grid box based on all WV SAR data acquired poleward of 40°S between 2016 and 2018. IB cases within the 40°-50°S latitude range are highlighted with blue dots, with red circles marking the prominent cases as shown in Fig. 2. The black dotted lines represent large iceberg tracks recorded in the NIC/BYU database.

the identified IB images on a 2° by 2° grid. The spatial distribution of IBs closely aligns with altimeter-derived estimates (Tournadre et al., 2012, 2016) and model simulations (Merino et al., 2016; Rackow et al., 2017). The entire Southern Ocean, poleward of 60°S, is populated by IBs, with three major longitudinal clusters located around 30°W, 140°W, and 115°E, where IB percentages reach approximately 35%, 25%, and 20%, respectively. The most prominent IB concentration is observed in the Southern Atlantic Ocean, spanning from 60°W to 30°E and between 50°S and 70°S, a region of frequent IB occurrences already identified by long-term ship observations (Orheim et al., 2023b). In the Southern Indian Ocean, IBs are predominantly found between 70°E and 130°E, with a clear tendency to extend toward the 60°S boundary. By contrast, in the Southern Pacific Ocean sector, from 80°W to 150°E, IBs are more spread and mostly poleward of 60°S.

The spatial distribution of the identified small icebergs only partially corresponds with the large

IB tracks recorded in the NIC/BYU database, as depicted by the black dotted curves in Fig. 7. Notable overlaps are observed, primarily in the northwestern Weddell Sea and sporadically across the Southern Pacific Ocean sector. Though a strong correlation between small IB fragments and nearby large icebergs is expected, the origins of these small IBs distanced from the larger icebergs remain underexplored. Tournadre et al. (2012) suggested these smaller IBs could drift over significant distances from their original calving sites, though this hypothesis lacks direct observational or modeling evidence (England et al., 2020). It is important to note that the NIC/BYU database only tracks IBs exceeding 6 km in length, with just 80 large icebergs recorded between 2016 and 2018. This represents a significant gap in IB monitoring, which is convincingly addressed using the systematic coverage provided by WV SAR data.

An interesting observation is the detection of 1,429 icebergs images within the latitudinal band of 40°S–50°S, as highlighted by the blue dots in Fig. 7. These findings suggest that IBs can cross the southern extratropics and arrive northward of 40°S, aligning with previous ship-based observations (Orheim et al., 2023b). Upon visual inspection of these IB images, 598 of them are found to contain noticeable-sized icebergs, while the remainder are predominantly small or in advanced stages of melting. Indicated by the red circles in Fig. 7, these 598 IBs are almost evenly distributed between 50°S and 40°S. This distribution suggests that the transport of freshwater from Antarctica via IBs might be quite efficient, spreading more effectively across the Southern Ocean than previously reported (Mackie et al., 2020; Rackow et al., 2017). Small-sized icebergs at the scale of 1 km, now identified by WV SAR imagery, provide valuable new sources to complement existing IB monitoring means, further offering visible features to facilitate the identification and tracking of IBs.

4.2. Temporal variability

The monthly distribution of total WV SAR acquisitions and corresponding identified icebergs is presented in Fig. 8 (a). S-1A consistently collects approximately 20,000 WV vignettes per month over the oceans south of 40°S. However, the number of detected IBs exhibits significant seasonal variability. The austral summer, particularly February, typically shows the highest IB counts, whereas the austral winter, notably July, records the lowest. For instance, the percentage of identified IBs in July remains relatively stable, around 0.65%, from 2016 to 2018, while February shows some fluctuations, with IB occurrence ranging from 7.7% in 2016 to 9.0% in 2017, and to 6.1% in 2018. This interannual variability in IB counts invites further investigations with a longer observational record to better identify the temporal trends. Note, these observed seasonal and

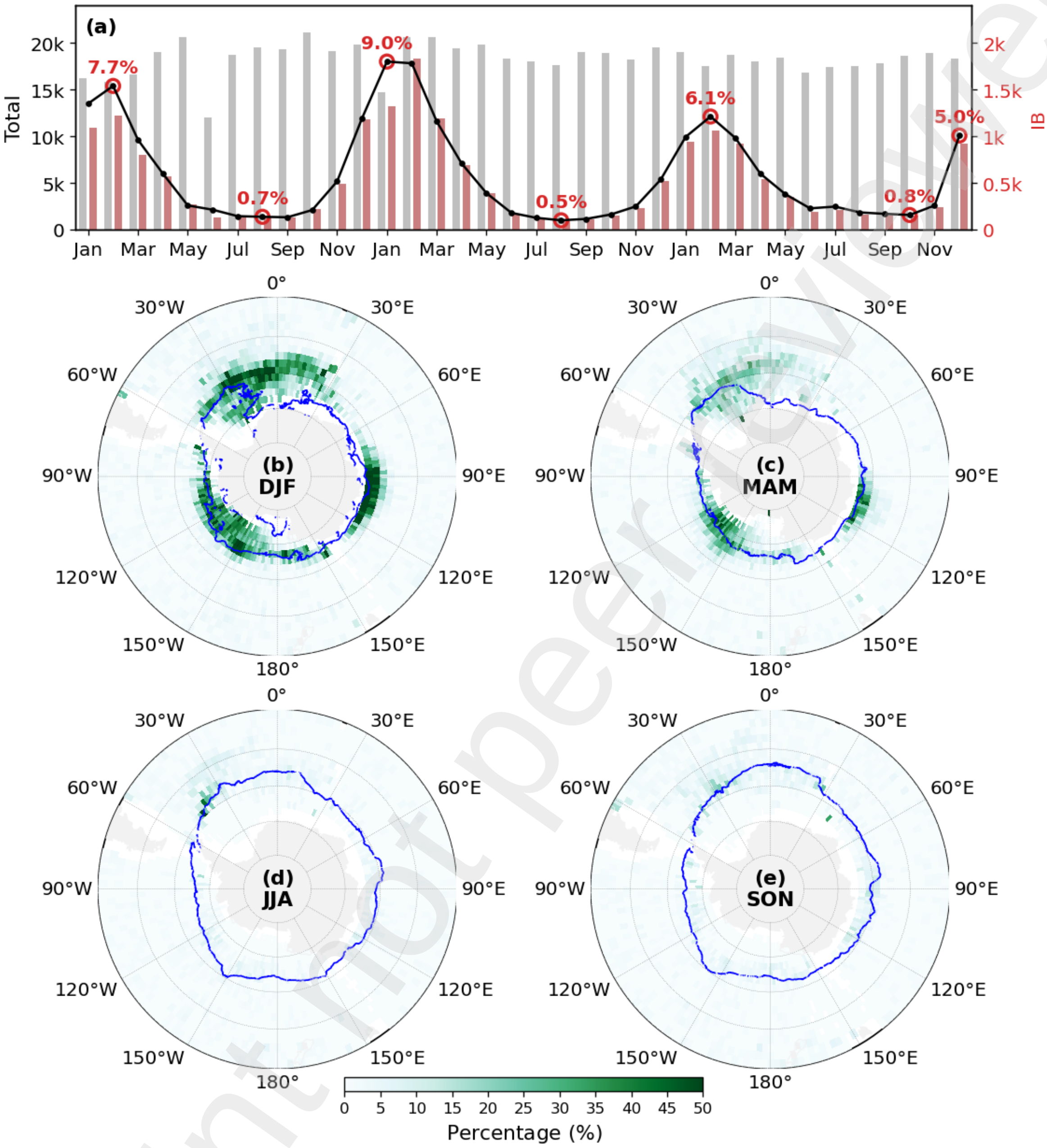

Fig. 8. (a) Monthly count of total WV vignettes (grey bar) and the detected iceberg (red bar) with the solid dark curve representing the IB percentages. Seasonal maps of IB percentage on 2° by 2° grid grouped by (b) DJF; (c) MAM; (d) JJA; (e) SON. The blue contour line corresponds to the ice concentration of 10% for rough indication of ice-water boundary.

interannual patterns again align well with IB occurrences derived from altimeter data, reported by Tournadre et al. (2012). Such variations are important to help examine the impact of Antarctic melting water trend on global climate and vice versa. It is worth pointing out that the IB counts should be considered rather than the number of identified IB images as their size and volume matter in the fresh water transport. These parameters are essential for accurately quantifying the melting water contribution from IBs to the Southern Ocean, which has significant implications for understanding the broader impacts of Antarctic ice melt on global climate.

Maps of the WV IB percentage on 2° by 2° grid for the four seasons of DJF, MAM, JJA and SON are given in Fig. 8 (b)-(e). The highest IB occurrence is observed during DJF, with maximum percentages exceeding 50%. The spatial distribution of IBs along the Antarctic coast is non-uniform, mirroring patterns observed in Fig. 7. IBs are primarily found south of 60°S, with the exception of the Southern Atlantic Ocean sector extending from 60°W to 30°E. During MAM, the IB occurrence is relatively lower, though it exhibits a distribution pattern similar to DJF. In contrast, IB presence is almost negligible during the austral winter months of JJA and SON. This seasonality highlights the austral summer as the primary period for IB formation. The sparse green spots on the JJA and SON maps likely correspond to named large IBs and their adjacent small fragments. It has been reported that many large IBs, such as those calved from the Antarctic Peninsula, drift under the influence of the Weddell Gyre and the Antarctic Coastal Current, as noted by (Collares et al., 2018). These large IBs are known to persist for several years, as illustrated in Fig. 7. Yet it is interesting that the small-sized IBs present on WV images also evidence this interannual variability.

In addition, the blue lines in Fig. 8 represent 10% ice concentration, marking the sea ice-water boundaries. The seasonal variation in these contours exhibits an inverse relationship with the distribution of WV-detected icebergs. During DJF, the sea ice extent is at its minimum, closely approaching the Antarctic continent, while the majority of identified IBs are distributed across open waters. As sea ice coverage expands from DJF through MAM and into JJA/SON, the population of IBs diminishes, and most of IBs are observed over sea ice. Icebergs are found over both open water and sea ice during the transitional season of MAM. This also evidences the capability of WV vignettes for monitoring icebergs under different conditions, which shall complement other satellite remote sensing, particularly in the detection and tracking of small icebergs in regions with diverse ice cover.

4.3. Correlation with named large icebergs

A current challenge further lies in the difficulty to link small icebergs with the named large ones. Bridging this gap requires a thorough assessment of IBs identified through WV SAR imagery with those detected by other satellite sources. A crucial step involves the joint analysis of

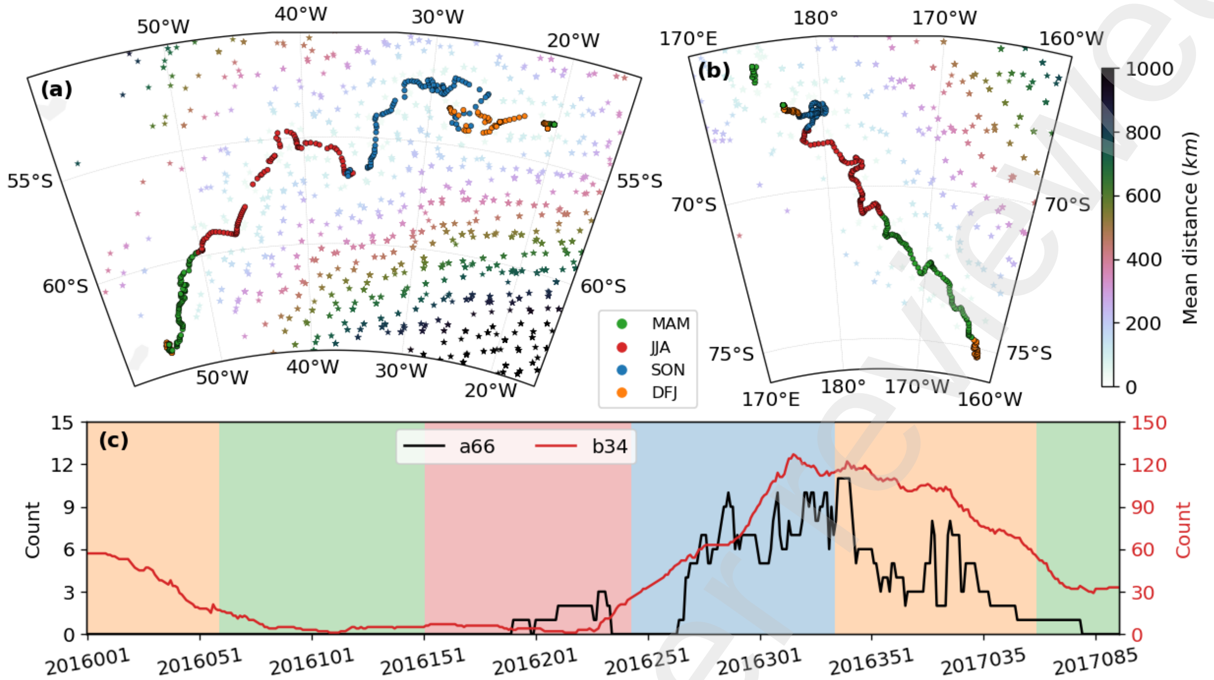

Fig. 9. (a)-(b) IB tracks of a66 and b34 given by the NIC/BYU database and positions of the detected WV IBs from 2016-01-01 to 2017-04-05. Positions of a66 and b34 are colored in four seasons of MAM (March-April-May), JJA (June-July-August), SON (September-October-November) and DJF (December-January-February. Color of WV IB indicates the distance to the closest large IB. (c) Count of identified IB images along with the a66 and b34 tracks with criteria of less than 500 km and 90 days.

medium-sized IBs using data acquired at different spatial resolutions, which would yield a more detailed understanding of their distribution patterns. As for this study, we select two IB tracks of a66 and b34 from the NIC/BYU database to manifest this aspect. Fig. 9 (a) and (b) illustrate the tracks of two large icebergs, a66 and b34, based on data from the NIC/BYU database, along with the positions of small icebergs detected by WV SAR during the period from January 1, 2016, to April 5, 2017. The tracks of a66 and b34 are displayed with colored dots representing four seasons: MAM (March-April-May), JJA (June-July-August), SON (September-October-November), and DJF (December-January-February). The trajectories of a66 and b34 are marked by an average daily travel speed of approximately 7.3 km/day and 6.9 km/day, respectively. These drifts are consistent with the general drift patterns of large icebergs within the Southern Ocean, driven by prevailing ocean currents and wind forces. The small icebergs identified by WV SAR are color-coded in terms of their mean distance to the nearest large iceberg. Most of SAR-detected small icebergs are located to the east of the large icebergs. This eastward distribution pattern indicates the prominent influence of the Antarctic Circumpolar Current (ACC). While the majority of small icebergs detected via WV SAR are concentrated to the east of the named large icebergs, a few notable exceptions appear to the west. These westward anomalies are speculated to have originated from the fragmentation of other large icebergs located further west than the primary iceberg under investigation.

Fig. 9 (c) shows the temporal variation in the number of small IBs detected near a66 (black line) and b34 (red line) over time. For both large icebergs, distinct seasonal patterns also appear, with small IB counts peaking in austral summer (DJF) and declining towards zero in the winter months. The highest counts for both a66 and b34 occur in November, indicating accelerated disintegration of the large icebergs as they drift from their calving locations to open waters. The zero counts observed at the beginning of the tracks reflect the lack of WV observations early in their lifecycles. The small fluctuations in the number of detected IBs along the tracks are likely influenced by local oceanic conditions, such as currents and interactions with the sea ice edge. While this analysis highlights the seasonal dependency of iceberg fragmentation, a more detailed investigation into the precise dynamics of small IB formation and drift, including iceberg size and shape extraction, remains to be performed, beyond the scope of this study.

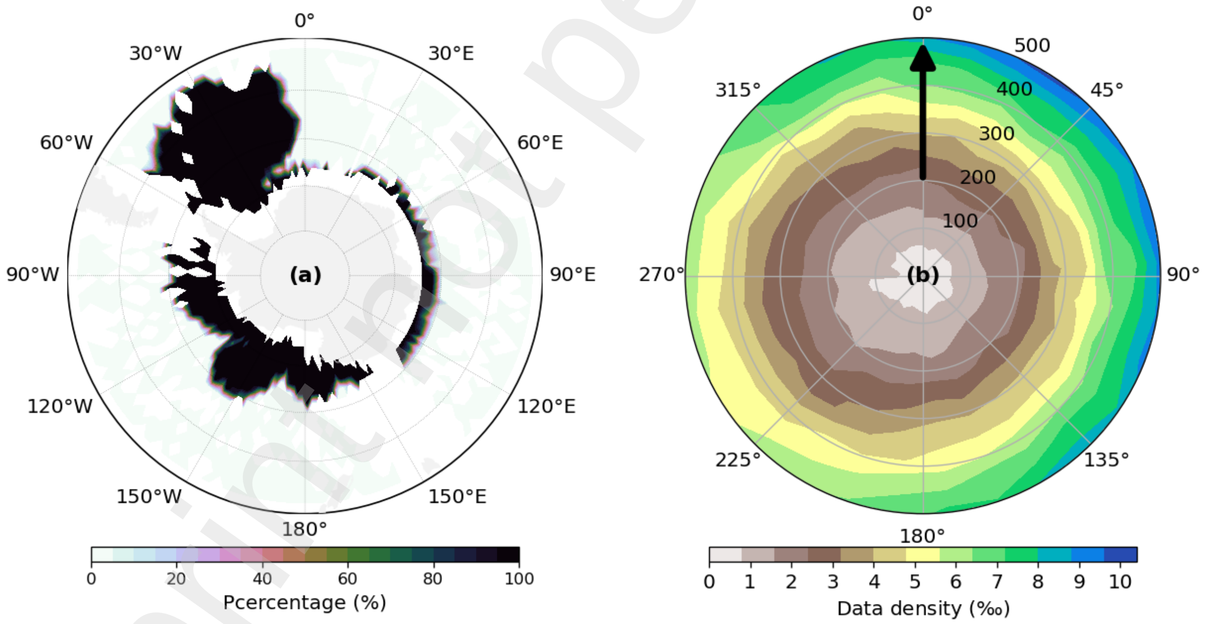

Fig. 10. (a) Proportion of collocated WV IBs to the closest NIC/BYU large IB over 2° by 2° grid. The criteria are less than 500 km and within 90 days. (b) Distribution of these collocated WV IBs relative to the large IB position and moving direction (indicated by the black arrow). The color represents binned data count over total number of WV IB.

Clearly, the named large icebergs reported by BYU/NIC provide crucial reference to build relationships with WV identified small-sized icebergs on the order of 1 km. This connection can be further explored by computing the distance from each identified WV SAR iceberg to its nearest large iceberg as given in Fig. 10 (a). Overall, 71.3% of the WV SAR-detected icebergs are located within 500 km and 90 days of a larger iceberg, this percentage decreasing to 37.2% when considering 200 km distance and 30 days. These icebergs are primarily concentrated in the northwestern Weddell Sea and near the Antarctic coast. Again consistent with previous results Tournadre et al. (2012), the small-sized iceberg cluster aligns with the tracks of large icebergs as in Fig. 7. Such a significant link between small and named large icebergs is consistent with the fragmentation of large icebergs into smaller ones, already extensively documented using satellite imagery (e.g. Braakmann-Folgmann et al., 2022; Huth et al., 2022). Combining the named large icebergs with the smaller ones identified by WV may thus help better monitor the calving process of a large iceberg.

Fig. 10 (b) illustrates the spatial distribution of collocated SAR-detected icebergs relative to the position and movement direction of large icebergs. The analysis is restricted to within 500 km of the large iceberg and a 90-day window. As expected, the number of WV-detected small IBs increases with increasing distance from the large iceberg, in line with the hypothesis that smaller icebergs are fragments, initially calved from the larger iceberg and subsequently drifting away. Over time and distance, these fragments accumulate. Note that a rightward bias is observed in the drift pattern of the small icebergs relative to the movement direction the linked large iceberg. Specifically, 29.3% of WV IBs are detected in the right front, and 26.8% in the right rear, compared to 23.5% and 20.4% in the left front and rear, respectively. This asymmetry likely reflects the influence of regional ocean circulation patterns, such as the Southern Ocean currents, the Antarctic Coastal Current, and the Weddell Gyre (Collares et al., 2018). For instance, large icebergs located between 0° and 90°W typically drift northward, while the prevailing ocean currents flow west to east, contributing to the observed rightward drift of small icebergs. In other words, the ability to track these small iceberg fragments using WV SAR imagery presents significant opportunities for better understanding of Southern Ocean circulation (Collares et al., 2018; Starr et al., 2021) and regional current dynamics (Huth et al., 2022).

5. Discussion and Conclusion

The WV vignettes offer unique capabilities for monitoring small-sized icebergs, primarily due to its high spatial resolution. reaching up to 5 meters. This fine resolution enables the detailed imaging of iceberg shapes, allowing for the detection of even the smallest icebergs that would otherwise go unnoticed by lower-resolution sensors. The detection of these small-sized icebergs marks a fundamental step in understanding their spatial distribution, drift patterns, and contribution to meltwater injection into the Southern Ocean. As a follow-up effort to Wang et al. (2019b), this study focuses on building a dedicated classification model to improve the identification of WV vignettes with icebergs. The Inception-v3 model is tuned to implement this task. The new classifier, termed as CMwvIB, is trained using 17400 expert-labelled images and validated across three independent hand-crafted datasets. MwvIB demonstrates very high performance, achieving precision and recall rates exceeding 90%. CMwvIB is opening new opportunities to build a new improved small iceberg climatology of the Southern Ocean with Sentinel-1 Wave Mode systematic acquisitions.

Misclassifications in the CMwvIB model are relatively few and can be categorized into two groups: false positives (NIB cases classified as IB by the model) and false negatives (IB cases classified as NIB by the model). The false positives are primarily attributed to small rain spots, ships, ice blocks, and strong convective events, which exhibit similar signatures to icebergs on SAR images. While the false negatives typically occur with small icebergs, in particular when they coexist with challenging environmental conditions such as sea ice, bio-slicks, low wind areas, and strong convection (e.g., heavy rains and convective cells). It is worth pointing out that the CMwvIB model faces significant limitations in identifying icebergs in sea ice regimes, as evidenced by the cases shown in Fig. 11. A detailed examination of a sub-track of WV vignettes acquired on 24 December 2016 (black dots) reveals four misidentified iceberg cases with clear sea ice textures, with their probabilities of being icebergs falling below 5% (see bottom panel of Fig. 6). This is largely due to the absence of similar sea ice environments in the training dataset (as discussed in Fig. 2 and Section 2.2). To mitigate these limitations, expanding the training set to include more sea ice cases and further refining the CMwvIB classifier could significantly improve detection accuracy. Multiple tagging is probably another way to help distinguish between icebergs in open water and sea ice environments given the distinct features of icebergs in these contrasting conditions. Incorporating auxiliary data, such as satellite-based ice concentration measurements may also be a practical approach to address these classification challenges.

The current CMwvIB model, while highly effective in detecting icebergs, also faces some limitations in accurately identifying iceberg positions and extracting associated shape descriptors, such as size and orientation. These limitations are particularly evident in complex SAR images, where icebergs are embedded within heterogeneous environments, such as sea ice, or are subject to varying backscatter intensities due to environmental factors (as demonstrated in Fig. 2 and

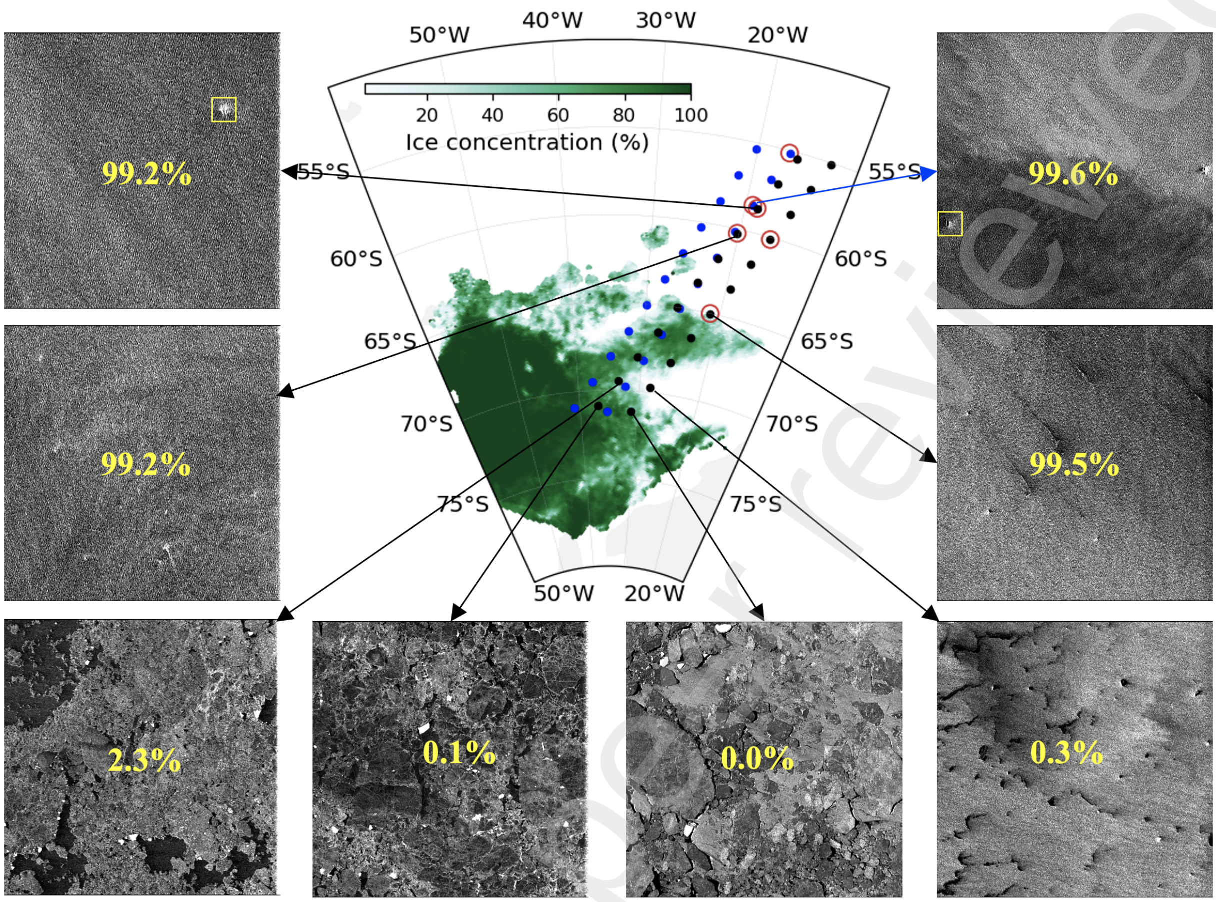

Fig. 11. Two sub-tracks of S-1 WV SAR images on 2016-12-22 in blue dots and 2016-12-24 in black dots. The six images of IBs over the open water that have been successfully identified by CMwvIB are marked in red circles. Four misclassified examples are illustrated over the sea ice. Percentages on each image are the IB probabilities calculated by CMwvIB and the two yellow boxes highlight one iceberg possibly being observed in different days.

Fig. 11). In our attempts to address these challenges, several traditional techniques, including local thresholding, texture segmentation, and object detection algorithms, were explored. However, these methods have not consistently produced reliable results in delineating iceberg shapes and positions, particularly for smaller icebergs or those with irregular geometries. This lack of precision highlights the need for further refinement in future work. A critical next step is to develop more robust algorithms that can accurately extract iceberg positions and sizes from individual SAR images. Efforts on implementing more dedicated techniques (e.g. Koo et al., 2023) or machine learning models (e.g. Zi et al., 2024) could significantly improve the detection of iceberg boundaries and their morphological features, enabling more detailed monitoring of iceberg dynamics and behavior.

But already, iceberg tracking seems to play a crucial role in understanding the relationship between named large icebergs and the smaller-sized icebergs identified through SAR imagery (see Fig. 10). Large icebergs, often tracked by satellite scatterometer and optical sensors, eventually break into smaller fragments that drift across the Southern Ocean. However, the detailed interactions between these large icebergs and their resulting fragments remain poorly understood. By employing SAR data for iceberg tracking, it is now possible to link the movement and evolution of small icebergs to their parent icebergs, offering new insights into the processes of calving, fragmentation, and drift. In addition, iceberg tracking that relies on accurate identification of iceberg position and shape could benefit from techniques similar to those used in eddy tracking (see yellow boxes in Fig. 11). Eddy tracking methods utilize sequential observations to follow the movement and evolution of mesoscale ocean features, which share some dynamic similarities with drifting icebergs. By applying similar principles, iceberg tracking could take advantage of continuous SAR observations and other spaceborne remote sensing to monitor the movement of both large and small icebergs over time.

The presence of icebergs equatorward of 50°S and even beyond 40°S (Fig. 7), as observed by S-1 WV SAR, offers a valuable complement to existing ship-based reports (Orheim et al., 2023b). Most icebergs detected at these latitudes are relatively small, typically with surface areas of less than 1 km^2 due to progressive melting. Such small icebergs may be documented through altimeter measurements (Tournadre et al., 2008), yet their frequency and distribution remain largely unexamined. The routine acquisition of WV SAR vignettes, coupled with the CMwvIB classifier, provides an opportunity to systematically monitor these icebergs and address this knowledge gap. Furthermore, joint investigations combining data from both S-1 WV and wide-swath SAR imaging mode, already extensively studied for iceberg detection (Barbat et al., 2021; Evans et al., 2023; Koo et al., 2023), should further enhance the identification of small icebergs. Other high resolution imaging radar measurements, i.e. from the Surface Water and Ocean Topography (SWOT) mission, are additionally expected to contribute to the detection of small icebergs. Still, with its long term continuing routine acquisition capability, S-1 WV data fully cover the Southern Ocean around the Antarctica every month (Fig. 1 and Fig. 7), to provide a sustained service for the next decades. Transfer learning between S-1 WV and the foreseen Earth Explorer 10 Harmony bi-static SAR mission or the new Copernicus ROSE-L will also be tested. Overall, systematic monitoring of IBs distribution and evolutions, with related investigations, shall hence be pursued to provide improved climate-scale records to monitor the Southern Ocean.

CRediT authorship contribution statement

Chen Wang: Conceptualization, Methodology, Formal analysis, Writing – original draft; Xiaoming Li: Conceptualization, Writing – review & editing, Supervision; Lijian Shi: Conceptualization, Writing – review & editing, Funding acquisition; Huimin Li: Methodology, Writing – review & editing, Visualization; Alexis Mouche: Writing – review & editing; Bertrand Chapron: Writing – review & editing.

Declaration of Competing Interest

The authors declare no known competing financial interests or personal relationships that could have appeared to influence the work reported in this paper.

Data availability

All original data used in this study are freely available with the links provided in the dataset section. The processed data and codes (in python) are available by request to the authors. We expect to implement our algorithm over all the S-1 WV SAR data and generate a publicly available IB database in the near future.

Acknowledgements

The authors are grateful to ESA, IFREMER and BYU/NIC for providing the S-1 WV SAR image, sea ice concentration and large iceberg track data. This work is supported in part by the National Natural Science Foundation of China (under grant of 42025605, 42206179 and 42350003), in part by the European Space Agency (under grant of 4000135827/21/NL–FF for Harmony Science Data Utilisation and Impact Study for Ocean, and 4000135998/21/i-BG for ESA Sentinel-1 Performance Center.

References

Alpers, W., Zhang, B., Mouche, A., Zeng, K., Chan, P.W., 2016. Rain footprints on C-band synthetic aperture radar images of the ocean - Revisited. Remote Sensing of Environment 187, 169–185. URL: https://linkinghub.elsevier.com/retrieve/pii/S003442571630387X, doi:10.1016/j.rse.2016.10.015.

Asiyabi, R.M., Ghorbanian, A., Tameh, S.N., Amani, M., Jin, S., Mohammadzadeh, A., 2023. Synthetic Aperture Radar (SAR) for Ocean: A Review. IEEE Journal of Selected Topics in Applied Earth Observations and Remote Sensing 16, 9106–9138. URL: https://ieeexplore.ieee.org/document/10234538/, doi:10.1109/JSTARS.2023.3310363.

Barbat, M.M., Rackow, T., Wesche, C., Hellmer, H.H., Mata, M.M., 2021. Automated iceberg tracking with a machine learning approach applied to SAR imagery: A Weddell sea case study. ISPRS Journal of Photogrammetry and Remote Sensing 172, 189–206. URL: https://linkinghub.elsevier.com/retrieve/pii/S0924271620303440, doi:10.1016/j.isprsjprs.2020.12.006.

Barbat, M.M., Wesche, C., Werhli, A.V., Mata, M.M., 2019. An adaptive machine learning approach to improve automatic iceberg detection from SAR images. ISPRS Journal of Photogrammetry and Remote Sensing 156, 247–259. URL: https://linkinghub.elsevier.com/retrieve/pii/S0924271619301996, doi:10.1016/j.isprsjprs.2019.08.015.

Biddle, L.C., Kaiser, J., Heywood, K.J., Thompson, A.F., Jenkins, A., 2015. Ocean glider observations of iceberg-enhanced biological production in the northwestern Weddell Sea. Geophysical Research Letters 42, 459–465. URL: http://doi.wiley.com/10.1002/2014GL062850, doi:10.1002/2014GL062850.

Braakmann-Folgmann, A., Shepherd, A., Gerrish, L., Izzard, J., Ridout, A., 2022. Observing the disintegration of the A68A iceberg from space. Remote Sensing of Environment 270, 112855. URL: https://linkinghub.elsevier.com/retrieve/pii/S0034425721005757, doi:10.1016/j.rse.2021.112855.

Braakmann-Folgmann, A., Shepherd, A., Ridout, A., 2021. Tracking changes in the area, thickness, and volume of the Thwaites tabular iceberg "B30" using satellite altimetry and imagery. The Cryosphere 15, 3861–3876. URL: https://tc.copernicus.org/articles/15/3861/2021/, doi:10.5194/tc-15-3861-2021.

Budge, J.S., Long, D.G., 2018. A Comprehensive Database for Antarctic Iceberg Tracking Using Scatterometer Data. IEEE Journal of Selected Topics in Applied Earth Observations and Remote Sensing 11, 434–442. URL: https://ieeexplore.ieee.org/document/8247260/, doi:10.1109/JSTARS.2017.2784186.

Collares, L.L., Mata, M.M., Kerr, R., Arigony-Neto, J., Barbat, M.M., 2018. Iceberg drift and ocean circulation in the northwestern Weddell Sea, Antarctica. Deep Sea Research Part II: Topical Studies in Oceanography 149, 10–24. URL: https://linkinghub.elsevier.com/retrieve/pii/S0967064517302485, doi:10.1016/j.dsr2.2018.02.014.

England, M.R., Wagner, T.J.W., Eisenman, I., 2020. Modeling the breakup of tabular icebergs. Science Advances 6, eabd1273. URL: https://www.science.org/doi/10.1126/sciadv.abd1273, doi:10.1126/sciadv.abd1273.

Evans, B., Faul, A., Fleming, A., Vaughan, D.G., Hosking, J.S., 2023. Unsupervised machine learning detection of iceberg populations within sea ice from dual-polarisation SAR imagery. Remote Sensing of Environment 297, 113780. URL: https://linkinghub.elsevier.com/retrieve/pii/S0034425723003310, doi:10.1016/j.rse.2023.113780.

Ezraty, R., Girard-Ardhuin, F., Piolle, J.f., Kaleschke, L., Heygster, G., 2007. Arctic & Antarctic sea ice concentration and Arctic sea ice drift estimated from Special Sensor MIcrowave data - User's manual V2.1.

Huth, A., Adcroft, A., Sergienko, O., Khan, N., 2022. Ocean currents break up a tabular iceberg. Science Advances 8, eabq6974. URL: https://www.science.org/doi/10.1126/sciadv.abq6974, doi:10.1126/sciadv.abq6974.

Jacka, T.H., Giles, A.B., 2007. Antarctic iceberg distribution and dissolution from ship-based observations. Journal of Glaciology 53, 341–356. URL: https://www.cambridge.org/core/product/identifier/S0022143000201044/type/journal_article, doi:10.3189/002214307783258521.

Jacobs, S., Helmer, H., Doake, C.S.M., Jenkins, A., Frolich, R.M., 1992. Melting of ice shelves and the mass balance of Antarctica. Journal of Glaciology 38, 375–387. URL: https://www.cambridge.org/core/product/identifier/S0022143000002252/type/journal_article, doi:10.3189/S0022143000002252.

Karvonen, J., Gegiuc, A., Niskanen, T., Montonen, A., Buus-Hinkler, J., Rinne, E., 2021. Iceberg detection in dual-polarized c-band sar imagery by segmentation and nonparametric cfar (snp-cfar). IEEE Transactions on Geoscience and Remote Sensing 60, 1–12.

Koo, Y., Xie, H., Mahmoud, H., Iqrah, J.M., Ackley, S.F., 2023. Automated detection and tracking of medium-large icebergs from Sentinel-1 imagery using Google Earth Engine. Remote Sensing of Environment 296, 113731. URL: https://linkinghub.elsevier.com/retrieve/pii/S0034425723002821, doi:10.1016/j.rse.2023.113731.

LeCun, Y., Bengio, Y., Hinton, G., 2015. Deep learning. Nature 521, 436–444. URL: http://www.nature.com/doifinder/10.1038/nature14539, doi:10.1038/nature14539. arXiv: 1312.6184v5 ISBN: 9780521835688.

Van der Maaten, L., Hinton, G., 2008. Visualizing data using t-SNE. Journal of machine learning research 9.

Mackie, S., Smith, I.J., Ridley, J.K., Stevens, D.P., Langhorne, P.J., 2020. Climate Response to Increasing Antarctic Iceberg and Ice Shelf Melt. Journal of Climate 33, 8917–8938. URL: https://journals.ametsoc.org/doi/10.1175/JCLI-D-19-0881.1, doi:10.1175/JCLI-D-19-0881.1.

Marino, A., Dierking, W., Wesche, C., 2016. A depolarization ratio anomaly detector to identify icebergs in sea ice using dual-polarization sar images. IEEE Transactions on Geoscience and Remote Sensing 54, 5602–5615.

Mazur, A., Wahlin, A., Krezel, A., 2017. An object-based sar image iceberg detection algorithm applied to the amundsen sea. Remote Sensing of Environment 189, 67–83. URL: https://linkinghub.elsevier.com/retrieve/pii/S0034425716304527, doi:10.1016/j.rse.2016.11.013.

Merino, N., Le Sommer, J., Durand, G., Jourdain, N.C., Madec, G., Mathiot, P., Tournadre, J., 2016. Antarctic icebergs melt over the Southern Ocean: Climatology and impact on sea ice. Ocean Modelling 104, 99–110. URL: https://linkinghub.elsevier.com/retrieve/pii/S1463500316300300, doi:10.1016/j.ocemod.2016.05.001.

Orheim, O., Giles, A.B., Jacka, T.H.J., Moholdt, G., 2023a. Quantifying dissolution rates of Antarctic icebergs in open water. Annals of Glaciology , 1–11URL: https://www.cambridge.org/core/product/identifier/S0260305523000265/type/journal_article, doi:10.1017/aog.2023.26.

Orheim, O., Giles, A.B., Moholdt, G., (Jo) Jacka, T.H., Bjørdal, A., 2023b. Antarctic iceberg distribution revealed through three decades of systematic ship-based observations in the SCAR International Iceberg Database. Journal of Glaciology 69, 551–565. URL: https://www.cambridge.org/core/product/identifier/S0022143022000843/type/journal_article, doi:10.1017/jog.2022.84.

Power, D., Youden, J., Lane, K., Randell, C., Flett, D., 2001. Iceberg Detection Capabilities of RADARSAT Synthetic Aperture Radar. Canadian Journal of Remote Sensing 27, 476–486. URL: http://www.tandfonline.com/doi/abs/10.1080/07038992.2001.10854888, doi:10.1080/07038992.2001.10854888.

Rackow, T., Wesche, C., Timmermann, R., Hellmer, H.H., Juricke, S., Jung, T., 2017. A simulation of small to giant A ntarctic iceberg evolution: Differential impact on climatology estimates. Journal of Geophysical Research: Oceans 122, 3170–3190. URL: https://agupubs.onlinelibrary.wiley.com/doi/10.1002/2016JC012513, doi:10.1002/2016JC012513.

Romanov, Y.A., Romanova, N.A., Romanov, P., 2012. Shape and size of Antarctic icebergs derived from ship observation data. Antarctic Science 24, 77–87. URL: https://www.cambridge.org/core/product/identifier/S0954102011000538/type/journal_article, doi:10.1017/S0954102011000538.

Romanov, Y.A., Romanova, N.A., Romanov, P., 2017. Geographical distribution and volume of Antarctic icebergs derived from ship observation data. Annals of Glaciology 58, 28–40. URL: https://www.cambridge.org/core/product/identifier/S0260305517000027/type/journal_article, doi:10.1017/aog.2017.2.

Schloesser, F., Friedrich, T., Timmermann, A., DeConto, R.M., Pollard, D., 2019. Antarctic iceberg impacts on future Southern Hemisphere climate. Nature Climate Change 9, 672–677. URL: http://www.nature.com/articles/s41558-019-0546-1, doi:10.1038/s41558-019-0546-1.

Schreier, M., Mannstein, H., Eyring, V., Bovensmann, H., 2007. Global ship track distribution and radiative forcing from 1 year of AATSR data. Geophysical Research Letters 34, 2007GL030664. URL: https://agupubs.onlinelibrary.wiley.com/doi/10.1029/2007GL030664, doi:10.1029/2007GL030664.

Silva, T.A., Bigg, G.R., 2005. Computer-based identification and tracking of Antarctic icebergs in SAR images. Remote Sensing of Environment 94, 287–297. URL: https://linkinghub.elsevier.com/retrieve/pii/S0034425704003268, doi:10.1016/j.rse.2004.10.002.

Smith, K., 2011. Free-drifting icebergs in the Southern Ocean: An overview. Deep Sea Research Part II: Topical Studies in Oceanography 58, 1277–1284. URL: https://linkinghub.elsevier.com/retrieve/pii/S0967064510003541, doi:10.1016/j.dsr2.2010.11.003.

Smith, R.M., Bigg, G.R., 2023. Impact of giant iceberg a68a on the physical conditions of the surface south atlantic, derived using remote sensing. Geophysical Research Letters 50, e2023GL104028. URL: https://agupubs.onlinelibrary.wiley.com/doi/abs/10.1029/2023GL104028, doi:https://doi.org/10.1029/2023GL104028.

Starr, A., Hall, I.R., Barker, S., Rackow, T., Zhang, X., Hemming, S.R., van der Lubbe, H.J.L., Knorr, G., Berke, M.A., Bigg, G.R., Cartagena-Sierra, A., Jiménez-Espejo, F.J., Gong, X., Gruetzner, J., Lathika, N., LeVay, L.J., Robinson, R.S., Ziegler, M., 2021. Antarctic icebergs reorganize ocean circulation during Pleistocene glacials. Nature 589, 236–241. URL: http://www.nature.com/articles/s41586-020-03094-7, doi:10.1038/s41586-020-03094-7.

Stuart, K., Long, D., 2011. Tracking large tabular icebergs using the SeaWinds Ku-band microwave scatterometer. Deep Sea Research Part II: Topical Studies in Oceanography 58, 1285–1300. URL: https://linkinghub.elsevier.com/retrieve/pii/S0967064510003553, doi:10.1016/j.dsr2.2010.11.004.

Szegedy, C., Liu, W., Jia, Y., Sermanet, P., Reed, S., Anguelov, D., Erhan, D., Vanhoucke, V., Rabinovich, A., 2015. Going deeper with convolutions, in: Proceedings of the IEEE conference on computer vision and pattern recognition, pp. 1–9.

Szegedy, C., Vanhoucke, V., Ioffe, S., Shlens, J., Wojna, Z., 2016. Rethinking the inception architecture for computer vision, in: Proceedings of the IEEE conference on computer vision and pattern recognition, pp. 2818–2826.

Torres, R., Snoeij, P., Geudtner, D., Bibby, D., Davidson, M., Attema, E., Potin, P., Rommen, B., Floury, N., Brown, M., Traver, I.N., Deghaye, P., Duesmann, B., Rosich, B., Miranda, N., Bruno, C., L'Abbate, M., Croci, R., Pietropaolo, A., Huchler, M., Rostan, F., 2012. GMES Sentinel-1 mission. Remote Sensing of Environment 120, 9–24. URL: https://linkinghub.elsevier.com/retrieve/pii/S0034425712000600, doi:10.1016/j.rse.2011.05.028. iSBN: 0034-4257.

Tournadre, J., Bouhier, N., Girard-Ardhuin, F., Rémy, F., 2016. Antarctic icebergs distributions 1992–2014. Journal of Geophysical Research: Oceans 121, 327–349. URL: https://onlinelibrary.wiley.com/doi/abs/10.1002/2015JC011178, doi:10.1002/2015JC011178.

Tournadre, J., Girard-Ardhuin, F., Legrésy, B., 2012. Antarctic icebergs distributions, 2002–2010. Journal of Geophysical Research: Oceans 117, 2011JC007441. URL: https://agupubs.onlinelibrary.wiley.com/doi/10.1029/2011JC007441, doi:10.1029/2011JC007441.

Tournadre, J., Whitmer, K., Girard-Ardhuin, F., 2008. Iceberg detection in open water by altimeter waveform analysis. Journal of Geophysical Research: Oceans 113, 2007JC004587. URL: https://agupubs.onlinelibrary.wiley.com/doi/10.1029/2007JC004587, doi:10.1029/2007JC004587.

Wang, C., Mouche, A., Tandeo, P., Stopa, J.E., Longépé, N., Erhard, G., Foster, R.C., Vandemark, D., Chapron, B., 2019a. A labelled ocean SAR imagery dataset of ten geophysical phenomena from Sentinel-1 wave mode. Geoscience Data Journal 6, 105–115. URL: https://onlinelibrary.wiley.com/doi/abs/10.1002/gdj3.73, doi:10.1002/gdj3.73. publisher: John Wiley & Sons, Ltd.

Wang, C., Tandeo, P., Mouche, A., Stopa, J.E., Gressani, V., Longepe, N., Vandemark, D., Foster, R.C., Chapron, B., 2019b. Classification of the global Sentinel-1 SAR vignettes for ocean surface process studies. Remote Sensing of Environment 234, 111457. URL: https://linkinghub.elsevier.com/retrieve/pii/S0034425719304766, doi:10.1016/j.rse.2019.111457. publisher: Elsevier.

Wesche, C., Dierking, W., 2012. Iceberg signatures and detection in SAR images in two test regions of the Weddell Sea, Antarctica. Journal of Glaciology 58, 325–339. URL: https://www.cambridge.org/core/product/identifier/S0022143000212069/type/journal_article, doi:10.3189/2012JoG11J020.

Wesche, C., Dierking, W., 2015. Near-coastal circum-Antarctic iceberg size distributions determined from Synthetic Aperture Radar images. Remote Sensing of Environment 156, 561–569. URL: https://linkinghub.elsevier.com/retrieve/pii/S0034425714004350, doi:10.1016/j.rse.2014.10.025.

Young, N., Turner, D., Hyland, G., Williams, R.N., 1998. Near-coastal iceberg distributions in East Antarctica, 50-145° E. Annals of Glaciology 27, 68–74. URL: https://www.cambridge.org/core/product/identifier/S0260305500017237/type/journal_article, doi:10.3189/1998AoG27-1-68-74.

Zi, N., Li, X.M., Gade, M., Fu, H., Min, S., 2024. Ocean eddy detection based on YOLO deep learning algorithm by synthetic aperture radar data. Remote Sensing of Environment 307, 114139. URL: https://linkinghub.elsevier.com/retrieve/pii/S0034425724001500, doi:10.1016/j.rse.2024.114139.